Design and Fabrication of Kidney Phantoms for Internal Radiation Dosimetry Using 3D Printing Technology

Johannes Tran-Gia, Susanne Schlögl, and Michael Lassmann

Department of Nuclear Medicine, University of Würzburg, Würzburg, Germany

Currently, the validation of multimodal quantitative imaging and absorbed dose measurements is impeded by the lack of suitable, commercially available anthropomorphic phantoms of variable sizes and shapes. To demonstrate the potential of 3-dimensional (3D) printing techniques for quantitative SPECT/CT imaging, a set of kidney dosimetry phantoms and their spherical counterparts was designed and manufactured with a fused-deposition-modeling 3D printer. Nuclide-dependent SPECT/CT calibration factors were determined to assess the accuracy of quantitative imaging for internal renal dosimetry. **Methods:** A set of 4 single-compartment kidney phantoms with filling volumes between 8 and 123 mL was designed on the basis of the outer kidney dimensions provided by MIRD pamphlet 19. After the phantoms had been printed, SPECT/CT acquisitions of 3 radionuclides (^{99m}Tc, ^{177}Lu, and ^{131}I) were obtained and calibration constants determined for each radionuclide–volume combination. A set of additionally manufactured spheres matching the kidney volumes was also examined to assess the influence of phantom shape and size on the calibration constants. **Results:** A set of refillable, waterproof, and chemically stable kidneys and spheres was successfully manufactured. Average calibration factors for ^{99m}Tc, ^{177}Lu, and ^{131}I were obtained in a large source measured in air. For the largest phantom (122.9 mL), the volumes of interest had to be enlarged by 1.2 mm for ^{99m}Tc, 2.5 mm for ^{177}Lu, and 4.9 mm for ^{131}I in all directions to obtain calibration factors comparable to the reference. Although partial-volume effects were observed for decreasing phantom volumes (percentage difference of up to 9.8% for the smallest volume [8.6 mL]), the difference between corresponding sphere–kidney pairs was small (<1.1% for all volumes). **Conclusion:** 3D printing is a promising prototyping technique for geometry-specific calibration of SPECT/CT systems. Although the underlying radionuclide and the related collimator have a major influence on the calibration, no relevant differences between kidney-shaped and spherically shaped uniform-activity phantoms were observed. With comparably low costs and submillimeter resolution, 3D printing techniques hold the potential for manufacturing individualized anthropomorphic phantoms in many clinical applications in nuclear medicine.

Key Words: anthropomorphic phantom design (kidney); 3D printing; internal radiation dosimetry; quantitative SPECT imaging; gamma camera calibration

J Nucl Med 2016; 57:1998–2005
DOI: 10.2967/jnumed.116.178046

The kidney represents the critical organ in many radionuclide therapies involving peptides or small molecules (*1–4*). An important prerequisite for reliable dosimetry based on planar and SPECT/CT images are measurements on quasirealistic anthropomorphic phantoms of a known activity concentration (*5–7*). However, industrial manufacturing of such phantoms is expensive and profitable only when large quantities are produced. Therefore, only a few phantoms representing very rough approximations of the underlying anatomies—in most cases an arrangement of simple geometric objects such as spheres and cylinders—are commercially available, impeding the validation of quantitative imaging and the related absorbed dose estimation based on patient- or even only organ-specific geometries.

After the introduction of stereolithography more than 2 decades ago (*8*), a wide range of rapid prototyping technologies (*9*) has evolved. More recently, some of these techniques have become commercially available under the term *3D printing* (*10,11*), enabling individual production of phantoms with more customized geometries and therefore offering an attractive alternative to industrial phantom construction. Most of the 3D printing setups recently proposed for phantom design are based on stereolithography (*12,13*), PolyJet (Stratasys Ltd.), or Multi Jet Fusion (HP Inc.) techniques (*14–16*). Although these photopolymerization-based 3D printing techniques feature the highest resolution that is currently commercially available (as low as ~20 μm), high investment costs in the 6-digit U.S. dollar range limit their application area to financially well-endowed research centers or commercial and therefore nonindividualized production.

To hold out the prospect for widespread use of 3D printing in clinical applications such as internal radiation dosimetry, the potential of the considerably more affordable fused deposition modeling (FDM) 3D printing technique (initial costs in the 4-digit U.S. dollar range) for manufacturing anthropomorphic phantoms was sounded out in this work. To assess the effect of the phantom geometry on quantitative SPECT/CT imaging, a set of kidney phantoms was designed on the basis of MIRD pamphlet 19 (*17*) and fabricated using an FDM-based 3D printer. Additionally, a set of volumetrically corresponding spheres, as typically used for SPECT calibration, was produced. Finally, SPECT/CT acquisitions of all combinations of radionuclides and age-models were performed with different radionuclides (^{99m}Tc, ^{177}Lu, and ^{131}I) to assess geometric effects as well as radionuclide and collimator dependence on the calibration constants obtained in a volume-of-interest (VOI) analysis.

MATERIALS AND METHODS

Design of Kidney Model Following MIRD Pamphlet 19

Simplified versions of 4 of the 6 age-dependent kidneys described in MIRD pamphlet 19 (*17*), with volumes of between 8 and 123 mL,

Received May 11, 2016; revision accepted Jun. 21, 2016.
For correspondence or reprints contact: Johannes Tran-Gia, Department of Nuclear Medicine, University of Würzburg, Oberdürrbacher Strasse 6, 97080 Würzburg, Germany.
E-mail: tran_j@ukw.de
Published online Jul. 21, 2016.

were used as kidney models in this work. The renal cortex was characterized by an ellipsoid with 2 half-axes of approximately the same size (a_{MIRD19} and c_{MIRD19}) as well as a shorter half-axis (b_{MIRD19}). A plane perpendicular to one of the longer half-axes represented the renal pelvis. To simplify the model and thereby the demand on the 3D printer, representations of the medullary pyramids were omitted in this work, reducing the initial multicompartment kidney to a single-compartment model. To additionally reduce the complexity of the computational 3D modeling, the ellipsoidal basic shape of the kidney was turned into a spheroid by averaging the 2 longer half-axes ($a_{new} = c_{new} > b_{new}$). The cut resembling the renal pelvis was performed at a distance d_{pelvis} from the origin. The MIRD19 and adapted kidney dimensions are given in Table 1.

Computational Modeling

Computer-aided designs (CADs) of the kidney models were created in Inventor Professional, version 2016 (Autodesk Inc.), using basic drawing commands (extrude, revolve, thicken, fillet). A wall thickness of 1.2 mm was applied to make the phantoms sufficiently rigid while minimizing the amount of filament used. The CAD models are depicted in Figure 1. To enable filling of the phantom, a cylinder of 17-mm height and 6-mm diameter was added to the top of each kidney model. Additionally, 2 cylinders of 6-mm diameter were added to both sides to fix the phantoms in PET body phantom L981602 (PTW-Freiburg). The completed CAD models were exported in the stereolithography interface format (STL).

In addition, 4 spheres matching the respective kidney volumes were constructed to validate the kidney phantoms against the spherical geometry typically used for calibration of SPECT/CT systems. After the kidney fill volumes (V_K) had been extracted using the Inventor Professional iProperties function, the radii (r_s) of the reference spheres were calculated according to $V_K \approx V_S = \frac{4}{3}\pi r_S^3$, where V_s is the volume of the reference spheres. On the basis of these radii, spheres were modeled in Inventor Professional using basic drawing commands (depicted in Supplemental Fig. 1; supplemental materials are available at http://jnm.snmjournals.org). The fill volumes and radii are given in Table 1.

Slicing and 3D Printing of Models

3D printing was performed using a Renkforce RF1000 3D printer (Conrad Electronic SE), which works by FDM. In this technique, a plastic filament is heated by an extrusion nozzle (Fig. 2A). The melted material is extruded onto a movable printing plate (Fig. 2B). As the filament hardens immediately after extrusion from the nozzle, an entire 3D object can be created by laying down successive layers of material. In this work, ExcelFil (Voltivo Group Ltd.) transparent polylactic acid (PLA) with a thickness of 3 mm was used as filament. These filaments lie in the range of 100–200 Hounsfield units (*18*).

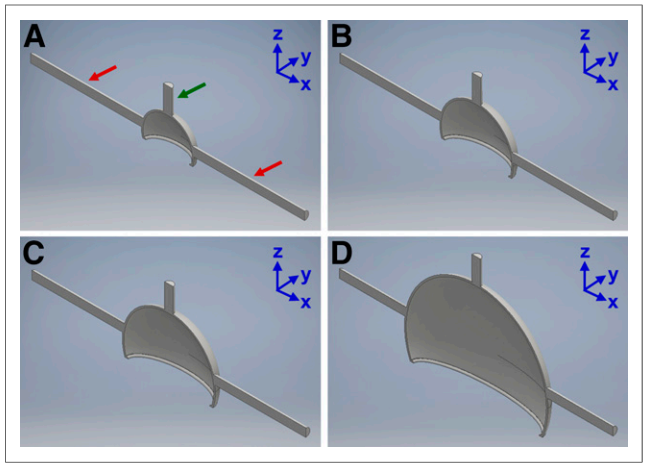

FIGURE 1. CAD models of renal cortices: newborn (A), 1-y-old (B), 5-y-old (C), and adult (D). Red arrows indicate cylinders added for attachment; green arrow, cylinder added for filling.

The printer was controlled through a personal computer using Repetier-Host, version 1.5.0. An embedded slicing software (Slic3r, version 1.2.9) takes the imported STL model and combines it with all necessary printing parameters (e.g., layer height, extrusion thickness, and number of perimeters per layer) to create the machine-readable G-code required for printing each layer. Supplemental Figure 2 shows an example of the slicing of the adult kidney and the corresponding sphere.

Because it is impossible to print overhangs or other horizontal parts without an underlying structure (such as the upper half of the spheres in Supplemental Fig. 1), support material, which is printed with a lower fill density, and which is only loosely attached to the main object, is added in the slicing procedure (Supplemental Fig. 2). To enable retrospective removal of the support material, each kidney was separated into renal pelvis and renal cortex (Supplemental Fig. 2A shows part of the sliced cortex without the pelvis). Similarly, the spheres had to be divided into halves (Supplemental Fig. 2B). Images of the procedure for 3D printing of the renal pelvis are shown in Figure 2.

After completion of printing, the support material was removed and the different components were agglutinated using a 2-component epoxy adhesive of medium viscosity (Loctite EA 3430; Henkel Ltd.). Subsequently, a filling hole of M1.2 was drilled into the filling cylinder, which was widened to M3.0 in the top half to make it sealable with a plastic screw and O-ring. Additionally, M6.0 thread profiles were cut at the ends of the attachment cylinders. Finally, the phantoms were coated

TABLE 1
Mathematic Parameters of Old (MIRD19) and New Kidney Models and Reference Spheres

Model	Parameter	Newborn	1-y-old	5-y-old	Adult
Kidney	a_{old} (mm)	17.9	26.1	32.0	45.0
	$b_{old} = b_{new}$ (mm)	9.3	12.5	14.0	15.0
	c_{old} (mm)	17.0	24.1	32.0	55.0
	$a_{new} = c_{new}$ (mm)	17.5	25.1	32.0	50.0
	d_{pelvis} (mm)	12.0	16.9	21.3	30.0
	V_K (cm^3)	8.59	24.15	44.36	122.93
Reference sphere	r_S (mm)	12.7	17.9	22.0	30.8
	V_S (cm^3)	8.58	24.23	44.30	122.99

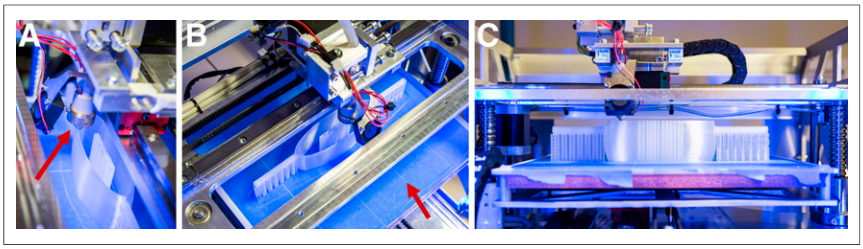

FIGURE 2. 3D printing process: extruder (arrow, A), movable printing plate (arrow, B), and profile (C).

with a low-viscosity epoxy casting resin (Epoxi-System E300GB; Breddermann Kunstharze) to ensure water tightness and chemical stability against the typically alkaline isotope solutions. A photograph of the final set of phantoms is given in Figure 3.

Attachment System for Body Phantom

An attachment system for the PET body phantom was printed to ensure easy insertion and removal of the kidney and sphere inserts. The associated CAD model is shown in Figure 4A. It includes 3 holes (width, M6.0) for height adjustment of the inserts within the body phantom. Additionally, it contains 4 screw holes (width, M4.0) for insertion of spacers to fix the attachment system to the body phantom's lid. 3D printing was performed using the same setup and parameters as described above. The attachment of the kidney insert is shown in Figure 4B: after the kidney insert was screwed into the bottom of the body phantom, 2 screw nuts (M6.0) were used to mount the attachment system. Finally, the 4 spacers were adjusted to fix the position of the lid before the phantom was closed.

Determination of Filling Weights

Before the measurements, all phantoms were weighed with a PCB 3500-2 precision mass scale (Kern & Sohn GmbH) with a readability of 0.01 g. Subsequently, they were filled with water and weighed again to determine the filling volumes and to ensure water tightness.

Preparation of Phantoms with Isotope Solution

In each experiment, one of the kidneys or spheres and a 100-mL plastic bottle were filled with a homogeneous isotope solution of a desired specific activity, a_{spec}. The isotope solution was produced by dissolving a highly concentrated radionuclide solution of a known activity, A_{total}, in a nonradioactive liquid. A_{total} was determined using a VDC-405 dose calibrator with a VIK-202 ionization chamber (Comecer SpA), which had previously been cross-calibrated to a high-purity germanium detector (HPGe; Canberra Industries Inc.) whose energy-dependent efficiency was calibrated with several NIST-traceable standards over the energy range considered. While ^{99m}Tc was combined with water, ^{177}Lu and ^{131}I were combined with 0.1 M HCl and 1 M NaOH, respectively, to keep the ions dissolved.

After the activity had been added to the liquid, the total weight $w_{solution}$ of the solution was obtained using the precision scale (difference between filled and empty container). After the activity A_{back} remaining in the syringe had been measured, the specific activity was calculated as follows:

$$a_{spec}(t_{ref}) = \frac{A_{total}(t_{ref}) - A_{back}(t_{ref})}{w_{solution}}. \quad \text{Eq. 1}$$

For consistency, all activities were recalculated to a reference time t_{ref}—typically the time of the initial activity measurement. After the kidney/sphere and the plastic bottle had been filled with the isotope solution, the kidney/sphere was attached to the body phantom, the rest of which was filled with water to emulate soft tissue. The plastic bottle was placed next to the phantom as a reference. Because there was no attenuation from surrounding materials such as acrylic glass or water, we call this reference bottle the "attenuation-free reference."

SPECT/CT Acquisition

SPECT/CT acquisitions of this setup were obtained using a Symbia T2 system (Siemens Healthineers) with a 15.9-mm-thick crystal.

First, the SPECT images were acquired using automatic contouring, a detector configuration of 180°, a pixel size (*px*) of 4.8 × 4.8 mm^2, a matrix size of 128 × 128, an acquisition time of 30 min, and 60 views. The collimators were chosen according to the isotope used in the respective acquisition (low-energy high-resolution for ^{99m}Tc, medium-energy low-penetration for ^{177}Lu, and high-energy for ^{131}I). After the SPECT acquisition, the CT images were acquired using 17 mAs, 130 kVp, a slice thickness of 5.0 mm, a field of view of 500 × 500 mm^2, and a matrix size of 512 × 512.

The SPECT images were reconstructed using an ordered-subsets expectation maximization algorithm with collimator-depth–dependent 3D resolution recovery (Flash 3D [Siemens Healthineers], 6 subsets, 6 iterations, and no filtering). Attenuation correction was based on the CT μ-maps. Scatter correction was performed using a double-energy window for ^{99m}Tc and a triple-energy window for ^{177}Lu and ^{131}I. The energy windows for the main emission photopeak and the adjacent lower and upper scatter energy windows are defined in Table 2.

Finally, CT acquisitions of an additionally printed 15 × 15 × 15 mm^3 PLA cube were obtained to determine the Hounsfield units of the PLA filament.

Determination of Calibration Factors

The calibration factor was determined as follows: CT-based VOIs were drawn using the provided software tool (syngo MI Applications, VA60C; Siemens Healthineers). Although ellipsoids with the theoretically known dimensions were used in the case of the spherical phantoms, layer-by-layer polygons were drawn for the more irregular shapes of the kidney and the reference bottle. On the basis of these VOIs, calibration factors were calculated by dividing the total number of counts by the activity at the start of the acquisition and the duration of the acquisition.

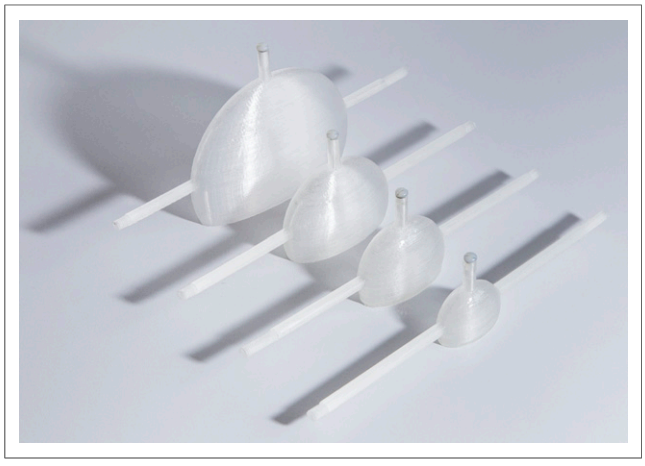

FIGURE 3. Manufactured set of kidney phantoms. From smallest to largest: newborn, 1-y-old, 5-y-old, and adult.

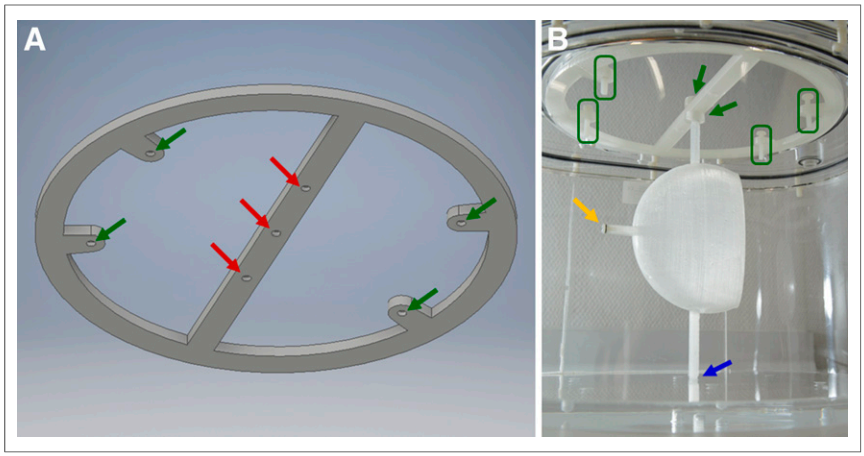

FIGURE 4. (A) CAD design of attachment system. Red arrows indicate option for height adjustment of kidneys; green arrows, holes for mounting spacers. (B) Attachment of kidney insert to body phantom. Yellow arrow indicates sealing screw; green arrows, screw nuts for mounting attachment system to kidney insert; green boxes, spacers for fixing position; blue arrow, location at which kidney insert is screwed into bottom of body phantom.

To compensate for spill-out effects caused by the limited resolution of the imaging system, all VOIs were extended by an isotope-dependent enlargement factor, Δρ, in all directions. The enlargement factor was determined separately for each isotope by matching the calibration factor of the largest sphere to the calibration factor of the associated reference bottle. By comparison of the radius of the corresponding sphere to the nominal radius, Δρ—defined as a multiple of *px*—was determined (e.g., $\Delta\rho = 0.5px$ for an enlargement by 2.4 mm for a *px* of 4.8 mm). This factor was subsequently applied to all other acquisitions of the associated isotope. All calibration factors given in this work were obtained using the enlarged VOIs.

RESULTS

Accuracy of 3D Printing Technique

Supplemental Table 1 shows the theoretic and measured filling volumes of all phantoms. To simplify the conversion, unit density was assumed.

The error between the filling volumes of the CAD design and the actual 3D printout increases with decreasing dimensions of the object (adult kidney and sphere, 2.4% and 0.5%, respectively; newborn kidney and sphere, 5.8% and 1.2%, respectively). Additionally, the error is considerably smaller for the spherical phantoms (maximum error of 1.2% for the smallest volume).

SPECT/CT Acquisition and Reconstruction

An average Hounsfield unit of approximately 142 was observed in the CT acquisition of the PLA cube.

The average (±SD) specific activities used for the calibration measurements were 0.90 ± 0.06 MBq/mL for ^{99m}Tc, 0.99 ± 0.05 MBq/mL for ^{177}Lu, and 0.26 ± 0.01 MBq/mL for ^{131}I. In this case, the SD describes the variation in specific activity between subsequent SPECT/CT acquisitions. These differences can be caused by radioactive decay of the isotope solution between subsequent SPECT/CT acquisitions (especially for ^{99m}Tc, with the shortest half-life), but they can also result from slight changes in the initial specific activity of the repeatedly prepared isotope solutions. Figure 5 shows the reconstructed SPECT/CT images and the VOIs used in the adult kidney phantom for the ^{177}Lu experiment and the corresponding spherical phantom for the ^{131}I experiment.

SPECT/CT Calibration

Table 3 shows the calibration factors determined from the enlarged VOIs for all kidneys and spheres, as well as the average of all reference bottle calibration factors for all isotope solutions. Considerable deviations of up to 9.8% from the attenuation-free reference were observed with decreasing volume. However, the percentage difference between spherical and kidney phantoms of comparable volume stayed below 1.1% for all ages and volumes.

The applied enlargement factors Δρ and the nominal and VOI radii and volumes are given in Table 4. Deviations from the ideal Δρ of the largest volume (adult column) can be attributed solely to inaccuracies in the VOI drawing. Although only a quarter of a voxel has to be added to the radius in the ^{99m}Tc acquisition, this factor increases to half a voxel for ^{177}Lu and even one voxel for ^{131}I.

The graphs of the calibration factors in Figure 6 illustrate the volume-dependent decrease in calibration factor, which is independent of the phantom geometry.

DISCUSSION

Assessment of 3D Printing Technique

In this work, FDM 3D printing was successfully used to manufacture a set of refillable, waterproof, and chemically stable phantoms. With a maximum volumetric deviation of about 6% between the CAD model and the final 3D object—even in case of the smallest kidney (volume, ~9 mL)—the printing accuracy was sufficient for SPECT/CT calibration measurements.

TABLE 2
Photopeak Energies and Lower and Upper Scatter Windows

Isotope	Photopeak (keV)	Width (%)	Lower scatter (%)	Upper scatter (%)
^{99m}Tc	140	15	15	
^{177}Lu	208	20	10	10
^{131}I	364	15	15	15

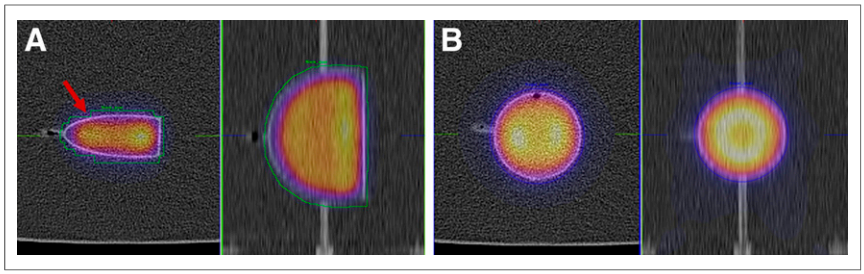

FIGURE 5. SPECT/CT reconstructions and VOIs used for determination of calibration factors for adult kidney filled with ^{177}Lu (A) and adult sphere filled with ^{131}I (B). Transitions between adjacent slices (arrow) can cause problems in VOI drawing: inclusion of too many counts from one slice has to be compensated for by including fewer counts in adjacent slices to minimize potential errors.

A large part of these deviations was caused by the major drawback of the single-extruder FDM 3D printing technique, namely the fact that horizontal layers or overhangs have to be underlaid by support material, making it necessary for many designs to be split into two parts, which are then separately printed (Supplemental Fig. 2B). In this case the seams have to be made thicker for better adhesion of the epoxy adhesive, potentially causing volume differences between the initial design and the actually printed object. This problem might be addressed by upgrading the 3D printing system to dual extrusion, in which a second extruder in combination with a second filament—typically with different chemical properties—is used to print support structures that can later be dissolved off the actual print. Although polyvinyl acetate, the most commonly used support material, is dissolvable in nothing but water, other filaments are dissolvable in more specific chemical solutions such as acetone (acrylonitrile butadiene styrene) or sodium hydroxide (PLA). As alkaline solutions—such as the 1 M NaOH used in case of the ^{131}I experiment in this work—are used for storage and transport of many radionuclides, PLA-based phantoms should always be coated with epoxy casting resin to prevent potential decomposition. In combination with the high layer bonding of PLA-printed objects (tensile strength ~57 MPa), the coating results in durable and chemically stable phantoms (*19*). Despite minor differences between the designed models and the final printed objects, the presented setup—with submillimeter layer height and in-plane resolution—holds the potential for the design and fabrication of a wide range of anthropomorphic phantoms for SPECT/CT and PET/CT imaging systems with a resolution in the range of several millimeters. Moreover, the wide range of filaments available for FDM 3D printing, with Hounsfield units from −60 to more than 3,000 (*18*), enables the emulation of almost every tissue of interest.

The size of objects to be 3D-printed is generally limited by the dimensions of the printer—in the case of FDM, the dimensions of the printing bed in combination with the vertical printer dimensions. Although these limitations are irrelevant for the kidney model of this study, they might be relevant if larger organs such as the liver, or even whole-body models, are to be printed (*20*).

SPECT/CT Calibration

Similar calibration factors were obtained for the attenuation-free reference and the largest phantoms (volume, ~120 mL). The volume-dependent decrease can be explained by an increasing influence of partial-volume effects for small volumes.

The increase in enlargement factor from ^{99m}Tc (low-energy high-resolution collimator: $<\Delta\rho> = 0.25px = 1.2$ mm) and

TABLE 3
Calibration Factors for Kidneys (CF_K), Spheres (CF_S), and Reference

Isotope	VOI	Newborn	1-y-old	5-y-old	Adult	Reference
^{99m}Tc	CF_K (MBq^{-1}s^{-1})	170.32	178.97	181.83	186.32	186.29 ± 2.26
	$\Delta_{K\text{-}Ref}$ (%)	8.6	3.9	2.4	0.018	
	CF_S (MBq^{-1}s^{-1})	169.16	178.20	182.06	186.34	
	$\Delta_{S\text{-}Ref}$ (%)	9.2	4.3	2.3	0.029	
	$\Delta_{S\text{-}K}$ (%)	0.69	0.43	0.13	0.011	
^{177}Lu	CF_K (MBq^{-1}s^{-1})	25.01	25.63	26.14	26.96	26.94 ± 0.08
	$\Delta_{K\text{-}Ref}$ (%)	7.2	4.8	3.0	0.089	
	CF_S (MBq^{-1}s^{-1})	24.77	25.59	26.12	26.95	
	$\Delta_{S\text{-}Ref}$ (%)	8.0	5.0	3.0	0.068	
	$\Delta_{S\text{-}K}$ (%)	0.96	0.17	0.052	0.021	
^{131}I	CF_K (MBq^{-1}s^{-1})	82.24	86.22	88.57	90.54	90.17 ± 0.59
	$\Delta_{K\text{-}Ref}$ (%)	8.8	4.4	1.8	0.41	
	CF_S (MBq^{-1}s^{-1})	81.33	85.76	88.28	90.40	
	$\Delta_{S\text{-}Ref}$ (%)	9.8	4.9	2.1	0.26	
	$\Delta_{S\text{-}K}$ (%)	1.1	0.53	0.33	0.16	

$\Delta_{K\text{-}Ref}$ = kidney percentage difference from attenuation-free reference; $\Delta_{S\text{-}Ref}$ = sphere percentage difference from attenuation-free reference; $\Delta_{S\text{-}K}$ = deviation between CF_S and CF_K.

TABLE 4

Nominal Radii ($r_{N,S}$), VOI Radii ($r_{VOI,S}$), Volumes ($V_{VOI,S}$, $V_{VOI,K}$), and Enlargement Factors (Δρ) for *px* of 4.8 Millimeters

Isotope	Parameter	Newborn	1-y-old	5-y-old	Adult	Average*
	$r_{N,S}$ (cm)	1.27	1.80	2.20	3.09	
^{99m}Tc	$r_{VOI,S}$ (cm)	1.39	1.92	2.32	3.20	
	Δρ (cm)	0.12	0.12	0.13	0.11	0.12 ± 0.01
	Δρ/*px*	0.25	0.26	0.27	0.24	0.25 ± 0.01
	$V_{VOI,S}$ (cm^3)	11.28	29.55	52.56	137.08	
	$V_{VOI,K}$ (cm^3)	12.99	33.61	58.27	161.38	
^{177}Lu	$r_{VOI,S}$ (cm)	1.54	2.04	2.44	3.33	
	Δρ (cm)	0.27	0.25	0.24	0.24	0.25 ± 0.01
	Δρ/*px*	0.56	0.52	0.50	0.50	0.52 ± 0.03
	$V_{VOI,S}$ (cm^3)	15.25	35.75	60.53	153.98	
	$V_{VOI,K}$ (cm^3)	19.82	44.56	75.47	216.73	
^{131}I	$r_{VOI,S}$ (cm)	1.76	2.29	2.69	3.56	
	Δρ (cm)	0.49	0.49	0.49	0.47	0.49 ± 0.01
	Δρ/*px*	1.03	1.03	1.02	0.99	1.02 ± 0.02
	$V_{VOI,S}$ (cm^3)	22.98	50.26	81.16	188.98	
	$V_{VOI,K}$ (cm^3)	27.56	55.86	97.47	229.38	

*Average over all ages for each isotope.

^{177}Lu (medium-energy low-penetration collimator: $<\Delta\rho> = 0.52px = 2.5$ mm) to ^{131}I (high-energy collimator: $<\Delta\rho> = 1.02px = 4.9$ mm) can be explained by the resolution of the collimators, which is deteriorating in this exact order ($<\cdot>$ indicates the averages as given in the last column of Table 4). As the spatial resolution of the imaging system largely depends on the collimator, spill-out effects play the largest role for the high-energy collimator with the worst resolution. Although the enlarged VOIs represent a reasonable correction of partial-volume effects for calibration measurements, care has to be taken in clinical settings when there is background activity or other structures near the target.

The difference in the volumes of the kidney and the spherical VOIs can be explained by the type of VOI that was chosen in the analysis. Although it is straightforward to draw an ellipsoidal VOI based on the diameter of the underlying sphere, it takes much more effort to draw a layer-by-layer polygon as was done for the irregular shapes of the kidneys. The main problem is that the size of the smallest kidney dimension (newborn: $b_{new} = 9.3$ mm) can be on the order of several voxels (*px* of 4.8 mm), and small changes in the positioning of the phantom relative to the patient bed may considerably affect the volume needed to include all relevant counts in a CT-based VOI. Additionally, transitions between adjacent slices can cause problems in the VOI drawing: inclusion of too many counts from one slice has to be compensated for by including fewer counts in the adjacent slice to minimize potential errors (Fig. 5A). For these reasons, the volumes of all kidney VOIs were 5%–30% larger than the volumes of the corresponding spherical VOIs.

In Figure 6, although, visually, there seem to be fewer partial-volume errors for the calibration factors of the kidney geometry than for the spheres, no relevant numeric differences were found (difference < 1.1%).

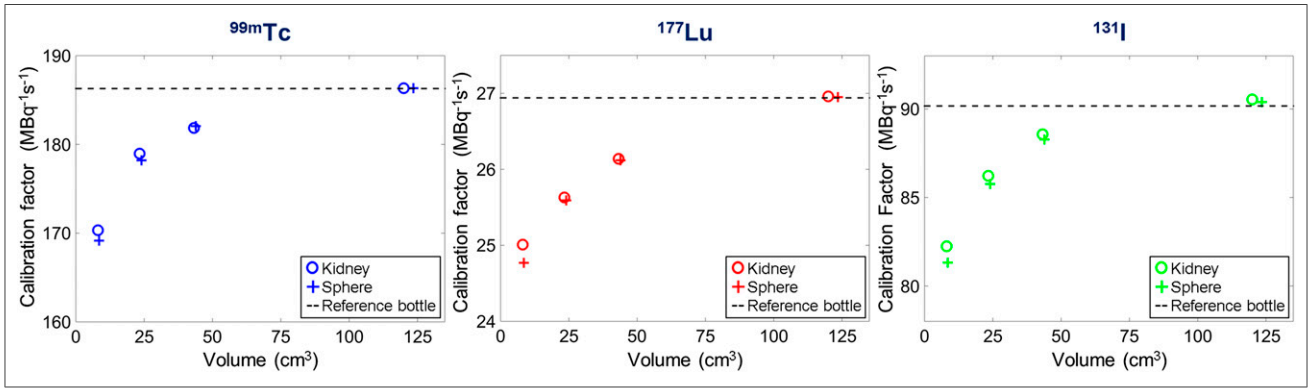

FIGURE 6. Volume-dependency of calibration factors obtained in kidneys, spheres, and reference bottle for 3 different radionuclides.

Comparison to Previously Presented Clinical Prototyping

The use of phantoms for the development and testing of clinical imaging modalities is widespread. Because of the nonavailability of anthropomorphic phantoms, most of the typically used phantoms consist of an arrangement of commercially available acrylic glass or silicone components mimicking organ function or morphology without, however, accurately modeling the shape or the structure of the organs themselves (*21*).

Recently, the commercial availability of various 3D printing modalities has created the possibility that phantoms can be individually manufactured for specific applications. In this context, commercially available phantoms reprinted using stereolithography (*13*) and Multi Jet Fusion 3D printing (*14*) were shown to be functionally equivalent for SPECT and PET quality controls. Similarly, the PolyJet 3D printing technique has been used to create models with pathologic entities to enhance the training experience of neurosurgeons (*16*) or develop patient-specific molecular imaging phantoms (*15*). These photopolymerization-based 3D printing techniques feature the highest resolution that is currently commercially available (600 × 600 dpi in layers of 16–32 μm), in turn leading to a very smooth surface finish. In contrast, the lower-resolving FDM technique (with layers no thinner than ~100 μm) can produce visible layer lines on the side walls, resulting in a rough surface finish, which—in this work— was compensated for by the coating. The major disadvantage of the photopolymerization-based techniques—and at the same time the greatest advantage of FDM printing—is of a financial nature. With a purchase price in the 6-digit U.S. dollar range, both the Objet500 Connex and the Objet Eden500V (Stratasys Inc.) used in some investigations (*15,16*) by far exceed the lower 4-digit price of the Renkforce RF1000 used in this work. The same applies to the ProJet 3500 HD (3D Systems Corp.), which was used in another investigation (*14*), with a purchase price in the higher 5-digit range. Together with a lower cost per printed volume, the FDM workflow presented in this work represents a serious low-cost alternative for manufacturing anthropomorphic or even patient-specific molecular imaging phantoms and might facilitate the application of 3D printing for clinical prototyping even in small clinics and research sites.

Limitations of and Possible Improvements to Single-Compartment Kidney Model

The single-compartment—or, equivalently, uniform-activity—kidney phantom designed in this study served a main purpose of demonstrating the general feasibility of SPECT quantification based on FDM-printed, anthropomorphic phantoms. From the results of this work, it can be concluded that PLA-based FDM 3D printing along with an epoxy coating enables the production of chemically stable, fillable phantoms that are sufficiently durable for SPECT/CT calibration studies. Although no significant differences in partial-volume effects were found between the kidney-shaped and the spherically shaped single-compartment phantoms, this conclusion will have to be reevaluated for more realistic kidney geometries, in which a low-activity inner region is typically surrounded by a ring of higher activity (*5*).

In a next step, a medullary compartment could be added to the simplified kidney model of this work. The resulting double-compartment kidney phantom would be fillable with nonuniform distributions of activity and therefore enable a more realistic analysis of partial-volume effects typically occurring in kidneys.

Although an increasing number of production steps (e.g., coating and agglutination of individually printed parts) would have to be incorporated, the setup could eventually be used to produce structures of high complexity—from multicompartment MIRD organs to patient-specific organ models obtained from MRI- or CT-based image data.

CONCLUSION

The presented 3D printing setup holds the potential for the design and fabrication of a wide range of quasirealistic anthropomorphic phantoms for testing and validation of internal radiation dosimetry. Despite comparably low initial and material costs, FDM-based techniques still hold the potential for printing 3D objects with submillimeter resolution, an accuracy sufficient with respect to the resolution of clinically available SPECT/CT and PET/CT systems.

In a calibration study, quantitative SPECT/CT acquisitions showed no relevant differences between the calibration constants of uniform-activity kidney designs derived from MIRD pamphlet 19 (*17*) and the additionally manufactured reference spheres as typically used to determine SPECT/CT calibration factors (difference $< 1.1\%$).

The setup could be used in the future to improve internal radiation dosimetry by calibrating SPECT/CT imaging systems for different MIRD organs or more sophisticated and even patient-specific organ models. Similarly, height-specific calibration factors for planar imaging could be derived for various geometries using the height-adjustable attachment system.

In a next step, more complex structures such as a medullary compartment could be added to the simplified kidney model of this work. In this manner, organ-specific distributions of radionuclide-labeled peptides or metabolites could be examined more comprehensively.

Ultimately, affordable 3D printing techniques could be combined with patient-specific MRI or CT data to establish reliable and reproducible quantitative imaging for individualized, patient-specific pre- or peritherapeutic internal radiation dosimetry of the kidneys or other critical organs.

DISCLOSURE

The costs of publication of this article were defrayed in part by the payment of page charges. Therefore, and solely to indicate this fact, this article is hereby marked "advertisement" in accordance with 18 USC section 1734. No potential conflict of interest relevant to this article was reported.

REFERENCES

1. Bodei L, Mueller-Brand J, Baum RP, et al. The joint IAEA, EANM, and SNMMI practical guidance on peptide receptor radionuclide therapy (PRRNT) in neuroendocrine tumours. *Eur J Nucl Med Mol Imaging.* 2013;40:800–816.
2. Lassmann M, Eberlein U. Radiation dosimetry aspects of ^{177}Lu. *Curr Radiopharm.* 2015;8:139–144.
3. Pfestroff A, Luster M, Jilg CA, et al. Current status and future perspectives of PSMA-targeted therapy in Europe: opportunity knocks. *Eur J Nucl Med Mol Imaging.* 2015;42:1971–1975.
4. Herrmann K, Schottelius M, Lapa C, et al. First-in-human experience of CXCR4-directed endoradiotherapy with ^{177}Lu- and ^{90}Y-labeled pentixather in advanced-stage multiple myeloma with extensive intra- and extramedullary disease. *J Nucl Med.* 2016;57:248–251.
5. Ljungberg M, Celler A, Konijnenberg MW, Eckerman KF, Dewaraja YK, Sjogreen-Gleisner K. MIRD pamphlet no. 26: joint EANM/MIRD guidelines

for quantitative ^{177}Lu SPECT applied for dosimetry of radiopharmaceutical therapy. *J Nucl Med.* 2016;57:151–162.
6. Dewaraja YK, Ljungberg M, Green AJ, et al. MIRD pamphlet no. 24: guidelines for quantitative ^{131}I SPECT in dosimetry applications. *J Nucl Med.* 2013;54: 2182–2188.
7. Dewaraja YK, Frey EC, Sgouros G, et al. MIRD pamphlet no. 23: quantitative SPECT for patient-specific 3-dimensional dosimetry in internal radionuclide therapy. *J Nucl Med.* 2012;53:1310–1325.
8. Hull A. Stereolithography as a tool for prototype molds. *Kunststoffe-German Plastics.* 1992;82:56–58.
9. Yan X, Gu P. A review of rapid prototyping technologies and systems. *Comput Aided Des.* 1996;28:307–318.
10. Durham M. Rapid prototyping: stereolithography, selective laser sintering, and polyjet. *Advanced Materials Processes.* 2003;161:40–42.
11. Graves A. Stereolithography vs. PolyJet: photopolymer 3D printing materials and applications. *R&D Magazine.* 2016;58:14–17.
12. Miller MA, Hutchins GD. Development of anatomically realistic PET and PET/CT phantoms with rapid prototyping technology. In: *2007 IEEE Nuclear Science Symposium Conference Record*. Piscataway, NJ: IEEE; 2007:4252–4257.
13. Hunt DC, Easton H, Caldwell CB. Design and construction of a quality control phantom for SPECT and PET imaging. *Med Phys.* 2009;36:5404–5411.
14. Bieniosek MF, Lee BJ, Levin CS. Technical note: characterization of custom 3D printed multimodality imaging phantoms. *Med Phys.* 2015;42:5913–5918.
15. Gear JI, Long C, Rushforth D, Chittenden SJ, Cummings C, Flux GD. Development of patient-specific molecular imaging phantoms using a 3D printer. *Med Phys.* 2014;41:082502.
16. Waran V, Narayanan V, Karuppiah R, Owen SL, Aziz T. Utility of multimaterial 3D printers in creating models with pathological entities to enhance the training experience of neurosurgeons. *J Neurosurg.* 2014;120:489–492.
17. Bouchet LG, Bolch WE, Blanco HP, et al. MIRD pamphlet no. 19: absorbed fractions and radionuclide S values for six age-dependent multiregion models of the kidney. *J Nucl Med.* 2003;44:1113–1147.
18. Lam K. MO-F-CAMPUS-I-03: CT and MR characteristics of some specialty 3D printing filaments. *Med Phys.* 2015;42:3579.
19. Tymrak BM, Kreiger M, Pearce JM. Mechanical properties of components fabricated with open-source 3-D printers under realistic environmental conditions. *Mater Des.* 2014;58:242–246.
20. Rengier F, Mehndiratta A, von Tengg-Kobligk H, et al. 3D printing based on imaging data: review of medical applications. *Int J Comput Assist Radiol Surg.* 2010;5:335–341.
21. SabbirAhmed AS, Demir M, Kabasakal L, Uslu I. A dynamic renal phantom for nuclear medicine studies. *Med Phys.* 2005;32:530–538.